Weierstraß-Institut
für Angewandte Analysis und Stochastik

Leibniz-Institut im Forschungsverbund Berlin e. V.

Preprint ISSN 2198-5855

Simulation and design of a compact GaAs based tunable dual-wavelength diode laser system

Jan-Philipp Koester[1], Mindaugas Radziunas[2], Anissa Zeghuzi[1], Hans Wenzel[1],

Andrea Knigge[1]

submitted: October 17, 2019

[1] Ferdinand-Braun-Institut
Leibniz Institut für Höchstfrequenztechnik
Gustav-Kirchhoff-Straße 4
12489 Berlin
Germany
E-Mail: jan-philipp.koester@fbh-berlin.de
anissa.zeghuzi@fbh-berlin.de
hans.wenzel@fbh-berlin.de
andrea.knigge@fbh-berlin.de

[2] Weierstrass Institute
Mohrenstr. 39
10117 Berlin
Germany
E-Mail: mindaugas.radziunas@wias-berlin.de

No. 2635
Berlin 2019

2010 *Mathematics Subject Classification.* 78A60, 35Q60, 78-04, 78A50.

Key words and phrases. Tunable laser diodes, dual-wavelength laser, traveling-wave model.

The authors want to thank H.-J. Wünsche for the discussions contributing to this work.

Edited by
Weierstraß-Institut für Angewandte Analysis und Stochastik (WIAS)
Leibniz-Institut im Forschungsverbund Berlin e. V.
Mohrenstraße 39
10117 Berlin
Germany

Fax: +49 30 20372-303
E-Mail: preprint@wias-berlin.de
World Wide Web: http://www.wias-berlin.de/

Simulation and design of a compact GaAs based tunable dual-wavelength diode laser system

Jan-Philipp Koester, Mindaugas Radziunas, Anissa Zeghuzi, Hans Wenzel, Andrea Knigge

Abstract

We present our design of a compact, integrated and tunable dual-wavelength diode laser system emitting around 785 nm, which is of interest for several applications like Raman spectroscopy and the generation of THz radiation. To achieve a more compact device compared to previous GaAs based designs two etch depths are realized, leading to shallowly etched ridge waveguides in regions were optical gain is applied and deeply etched waveguides used to enable compact integrated waveguide components. The device parameters are optimized using a numerically efficient simulation tool for passive waveguides. Subsequently, the entire laser system is further analyzed applying a sophisticated traveling-wave equation based model for active devices giving access to internal intensity and carrier density distributions. It is shown that active laser simulations are crucial to deduce critical and performance limiting design aspects not accessible via an all-passive simulation.

1 Introduction

Tunable multi-wavelength GaAs based diode lasers emitting in the wavelength range between 630 nm and 1.1 µm are of interest for several applications, for example Raman spectroscopy (785 nm) [1], water vapor sensing (965 nm) [2] and the generation of THz radiation (785 nm and 850 nm) [3, 4].

One possibility to achieve multi-wavelength emitting devices is to integrate two or more distributed feedback (DFB) or distributed Bragg reflector (DBR) lasers having different emission wavelengths next to each other on one chip and to couple their emission into one common output waveguide. In context of the InP material system which is used to realize laser diodes emitting at 1.55 µm multi-step epitaxy as well as heterogeneous integration are common fabrication methods. Those techniques, however, are not easily transferable to the GaAs material system.

Our approach to fabricate tunable multi-wavelength lasers based on GaAs avoids any multi-step epitaxy. Here, the active region extends over the whole chip. The functionality of the different parts such as laser, amplifiers, waveguides and couplers are defined by etching parts of the chip surface and choosing appropriate contact layouts. Tuning is achieved by micro-heaters placed next to the wavelength selective gratings [5].

In previous designs the etch depth of the ridge waveguides (RWs) was the same over the entire chip resulting in a 2000 µm long waveguide coupler [1]. To make the coupler section more compact we propose a new design based on two etch depths. The regions where optical gain is supplied (lasers and amplifiers) are shallowly etched to ensure fundamental lateral mode operation. In contrast, the coupler section is deeply etched to provide a strong lateral confinement.

Following this approach we present a simulation based design of a compact and tunable dual-wavelength diode laser emitting around 785 nm. First, we present the underlying design idea, the waveguide

DOI 10.20347/WIAS.PREPRINT.2635 Berlin 2019

structure under study and all needed integrated waveguide components in Section 2. Subsequently, the simulation tools used are introduced in Section 3. The results of passive and active simulations are shown in Section 4 and 5, respectively. Finally, the conclusion is given in Section 6.

2 Design approach

Our new lateral-longitudinal design approach is schematically shown in Fig. 1. Here, the regions depicted in bright gray correspond to shallowly etched areas, whereas deeply etched regions are indicated by dark gray. The corresponding transverse cross sections are depicted in the upper part of Fig. 1. The design can be divided into three main sections. Starting from the left, a multi-channel section (MCS), a coupler section (CS) and a front section (FS). The MCS contains unbiased DBRs providing the spectrally filtered feedback of each arm and biased RWs. The CS connects all channels to one common output. This is achieved using different integrated waveguide components (see Section 2.2). The FS contains only one RW resulting in a single aperture at the front facet. Note that different bias voltages can be applied to individual parts of the waveguide.

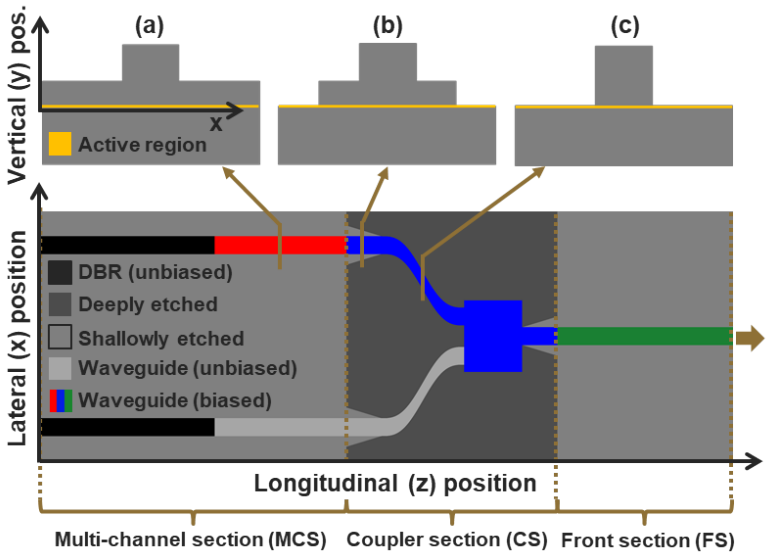

Figure 1: Bottom: Lateral-longitudinal (x,z) plane of the device under study indicating its three different sections. The arrow on the right hand side indicates the emitting front facet. Top: Vertical-lateral (y,x) cross sections at different longitudinal positions. (a) Shallow-etched low confinement waveguide; (b) Waveguide taper; (c) Deep-etched high confinement waveguide

2.1 Waveguide structure

The used vertical structure including thickness, material index and absorption coefficient of each layer is summarized in Table 1. Here, layer No. 0 corresponds to silicon nitride which is used to fill the etched trenches needed to form a ridge waveguide. Note that the vertical waveguide is designed to support only the fundamental vertical mode. To study approximately lateral waveguide effects the effective index method can be used [6]. Following this approach, Fig. 2 (a) shows the effective-index step $\Delta n_{\mathrm{eff}} = n_{\mathrm{eff,r}} - n_{\mathrm{eff,t}}$ as function of the residual layer thickness d_{res}. Here, $n_{\mathrm{eff,r}}$ and $n_{\mathrm{eff,t}}$ are the effective indices of the vertical mode of the ridge and trench regions, respectively. In what follows the shallowly and deeply etched areas were chosen to be $d_{\mathrm{res,s}} = 0.5$ µm and $d_{\mathrm{res,d}} = 0$ µm corresponding to $\Delta n_{\mathrm{eff,s}} = 3 \cdot 10^{-3}$ and $\Delta n_{\mathrm{eff,d}} = 3 \cdot 10^{-2}$, respectively. Fig 2 (b) shows the confinement factor $\Gamma_{\mathrm{lat}} = \int_{-w_{\mathrm{r}}/2}^{w_{\mathrm{r}}/2} |u(x)|^2 \mathrm{d}x / \int_{-\infty}^{\infty} |u(x)|^2 \mathrm{d}x$ of the first three lateral modes as function of the residual layer thickness with w_{r} being the ridge width and u the mode profile. It can

Table 1: Vertical waveguide layer structure

Layer No.	Function	Thickness / µm	Material index	Absorption / cm^{-1}
0	Insulation	$1.5 - d_{\text{res}}$	1.950	0.0
1	p-Cladding	0.6	3.192	21.0
2	p-Cladding	0.2	3.193	7.0
3	p-Cladding	0.2	3.193	3.5
4	p-Confinement	0.2	3.224	3.5
5	p-Confinement	0.2	3.224	1.4
6	p-Confinement	0.1	3.224	0.7
7	Active region	0.034	3.457	0.0
8	n-Confinement	0.2	3.224	0.3
9	n-Confinement	0.3	3.224	0.6
10	n-Cladding	0.2	3.193	1.5
11	n-Cladding	1.0	3.193	3.0

be seen that the shallow-etched RW supports one mode whereas the deep-etched RW supports three lateral guided modes. This indicates the importance of properly designed integrated waveguide components to avoid the excitation of higher order modes.

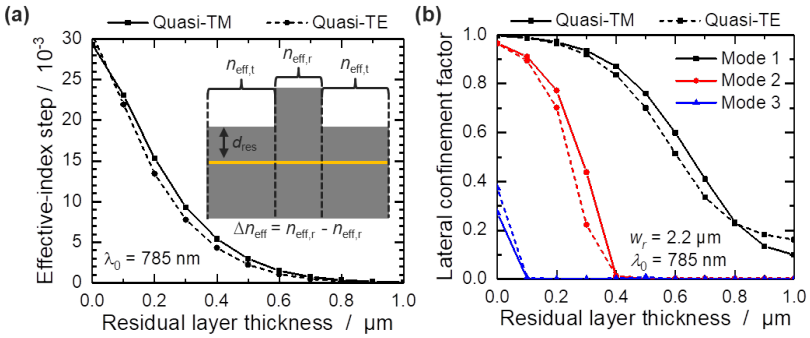

Figure 2: (a) Effective-index step as function of the residual layer thickness d_{res}. (b) Lateral confinement factor of a RW with $w_{\text{r}} = 2.2$ µm as function of d_{res}.

2.2 Integrated waveguide components

The CS (see Fig. 1) consists of three different integrated waveguide components: First, mode-size converters formed by lateral tapers connect the shallowly and deeply etched regions. Second, S-bends are used to change the lateral offset between different laser arms. Third, a multi-mode interference (MMI) coupler combines all laser channels to one common output waveguide. In the following all components are described in more detail.

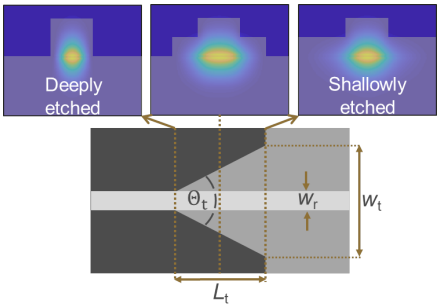

Figure 3: Bottom: Schematic 2D (x,z) representation of a lateral mode-size converter including the relevant design parameters. Top: Fundamental transverse waveguide mode of different cross-sections (x,y)

The goal of the lateral mode-size converters is to adiabatically change the mode profile of the fundamental mode between low and high confinement waveguides without exciting higher order or radiative modes. This is done by keeping the waveguide width constant and linearly changing the width of the shallow etching. A schematic representation of the taper including relevant design parameters, namely ridge width w_{r}, taper width w_{t} and taper length L_{t}, is shown in Fig. 3. The upper part of the figure, showing the transverse fundamental mode profile at three longitudinal positions of the mode-size converter, illustrates its working principle.

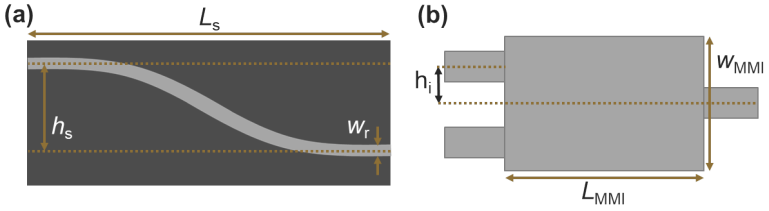

Figure 4: Schematic 2D (x,z) representations of (a) the sine S-bend and (b) the multi-mode interference coupler including their relevant design parameters.

At the entrance to the CS, the lateral offset between the two arms is $2(h_s + h_i)$, where $2h_i$ is the channel offset at the entrance to the MMI coupler, see Fig. 3 (c). The offset reduction is achieved using a pair of sine S-bends [7] described by

$$x(z) = \pm \left[h_i + h_s \left(1 - \frac{z}{L_s} + \frac{1}{2\pi} \sin\left(\frac{2\pi z}{L_s} \right) \right) \right] \tag{1}$$

where h_{s} and $L_{\mathbf{s}}$ are the single S-bend lateral offset and S-bend length, respectively. A schematic 2D representation of the S-bend is shown in Fig. 4 (a). As mentioned before, the waveguide within the CS supports higher order modes. To avoid the excitation of those modes the S-bend design has to be adiabatic, meaning a good fundamental mode overlap has to be ensured within the entire device restricting its minimal length.

The coupler combines all channels to one common output waveguide. In previous designs this has been done using Y-branches [1]. Enabled by the increased index step of the deep-etched CS we are applying a MMI coupler instead. Fig. 4 (b) shows a schematic 2D representation of a 2x1 MMI coupler introducing its design parameters MMI length L_{MMI}, MMI width w_{MMI} and the half input waveguide offset h_i.

3 Simulation tools

Our simulation procedure is split into two stages. First, we use a versatile and numerically efficient passive but rigorous waveguide simulation tool to optimize the components introduced in Section 2. Afterwards, the resulting system consisting of optimized components is analyzed using an active laser model. Below, both simulation tools are explained in more detail.

3.1 Passive waveguide simulation tool

The passive waveguide simulations were carried out using FIMMPROP as part of the commercial software FIMMWAVE from Photon Design [8]. In its most general form it provides a rigorous and fully vectorial solution of Maxwell's equations in frequency domain based on the eigenmode expansion method [9]. Here, the field in each longitudinal invariant dielectric slice of the simulated device is

described as superposition of N_{m} forward and backward traveling guided and radiated modes. To calculate those modes the program offers real and complex vectorial and semi-vectorial mode solvers using different numerical schemes.

All our simulations were performed using a finite-difference semi-vectorial quasi-TM mode solver in the transversal (y,x) plane. The simulation parameter presented here were determined performing convergence tests, resulting in a simulation domain width W of 12.2 µm for taper and S-bends and 22.2 µm for MMI coupler simulations. The number of modes N_{m} varied between 40 and 50. To simulate the mode-size converter and MMI coupler the spatial discretization was set to $dx = 0.04$ µm and $dy = 0.01$ µm, whereas a non-uniform mesh was applied for the simulations of S-bends. The latter was modeled dividing the bend in 40 equally spaced sections of constant curvature represented in cylindrical coordinates.

3.2 Active device simulation tool

The active laser simulations are performed using WIAS-BALaser [10]. Its optical model provides an approximated solution of Maxwell's equations in the time domain [11]. The forward and backward propagating slowly varying fields $u^{\pm}(x,z,t)$ within the longitudinal-lateral (z,x) plane are described by a paraxial traveling wave equation

$$\frac{n_{\mathrm{g}}}{c_0}\partial_t u^{\pm} \pm \partial_z u^{\pm} = -\frac{i}{2\bar{n}k_0}\partial_x^2 u^{\pm} - ik_0\kappa u^{\mp} - i\Delta\beta u^{\pm} - \mathcal{D}(z)u^{\pm} + f_{\mathrm{sp}}^{\pm} \tag{2}$$

where n_{g} is the group index, c_0 the speed of light in vacuum, $\bar{n}$ the reference index, k_0 the free-space propagation constant, κ the coupling coefficient between forward and backward traveling waves used to model Bragg gratings, $f_{\mathrm{sp}}^{\pm}$ are the stochastic forces accounting for spontaneous emission [12] and $\mathcal{D}$ an operator describing the gain dispersion using a Lorentzian approximation [13, 14]. The relative effective propagation factor $\Delta\beta$ depends on the local excess carrier density $N(x,z,t)$ [14].

The excess carrier density N is obtained from the solution of the effective diffusion equation

$$\partial_t N = \partial_x\left[D_{\mathsf{eff}}(N)\partial_x N\right] + \frac{j}{ed} - R \tag{3}$$

where D_{eff} is an effective diffusion coefficient, j the injected current density into the active region (AR), e the elementary charge and d the quantum well thickness. The recombination rate R accounts for nonradiative, spontaneous radiative and stimulated recombinations. The carrier transport is calculated in every time step for each longitudinal position. Current spreading within the vertical-lateral domain of the p-doped region is described by a Laplace equation for the quasi-Fermi potential of the holes φ_{p} with σ_{p} being the electrical conductivity,

$$\nabla\left[\sigma_{\mathrm{p}}\nabla\varphi_{\mathrm{p}}\right] = 0. \tag{4}$$

It is assumed that the current flow is continuous at the interfaces of layers and vanishes at all outer surfaces except the p-contact stripe. The potential is set to be $\varphi_{\mathrm{p}} = U_0$ and $\varphi_{\mathrm{p}} = \varphi_{\mathrm{F}}(N)$ at the p-contact and at the boundary to the AR, respectively. The current flux into the AR defines the injected current entering (3), $j = -\sigma_{\mathrm{p}}\partial_y\varphi_{\mathrm{p}}|_{@\mathsf{AR}}$.

BALaser also resolves a sophisticated heat model, where the temperature distribution and thermally induced changes of the refractive index distributions are calculated iteratively solving a stationary heat flow equation for the self-consistent time averaged heat sources within each vertical-lateral cross

section [15]. In this work it is assumed that thermal effects play a negligible role, therefore, the heat model was not used.

All BALaser simulations were performed using a longitudinal and lateral spatial discretization of $\Delta z = 0.5$ µm and $\Delta x = 0.05$ µm, respectively, leading to a temporal step of $\Delta t = \frac{\Delta z n_\mathrm{g}}{c_0} \approx 6.25$ fs. The total simulation time was chosen to be $T_\mathrm{sim} = 3$ ns, where time averaged results were calculated during the last nanosecond.

3.3 Comparison of the simulation tools

Splitting the design process into two stages requires a good agreement between the optical fields provided by both simulation tools. This, however, is not self-evident since the optical models rely on different mathematical assumptions. Fig. 5 shows the field intensity of the forward propagating wave within a MMI coupler obtained by BALaser as well as (z,x) and (z,y,x) FIMMPROP simulations, where the first two rely on the effective index method. In this specific example the fundamental mode of the upper left arm is coupled into the multi-mode section of a 2x1 MMI coupler (cf. Fig. 4 (b)). Besides the good qualitative agreement of the results it can be seen that not all light is coupled into the right hand side output waveguide. It is known that 2^qx1 MMI, similar to Y-couplers, have an insertion loss of $3 \cdot q$ dB, where q is a positive integer.

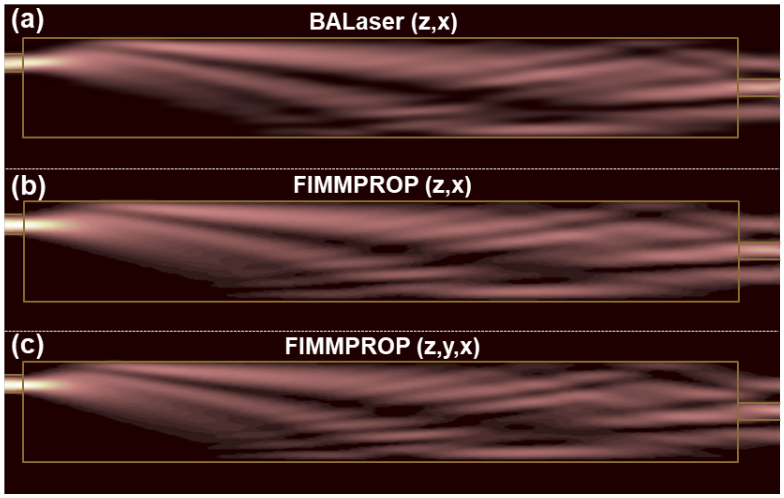

Figure 5: Field intensity within a 2x1 MMI coupler obtained by (a) BALaser, (b) (z,x) FIMMPROP and (c) (z,y,x) FIMMPROP simulations.

4 Passive waveguide simulations

In what follows the optimization of all integrated waveguide components within the CS regarding low losses of the fundamental mode and negligible excitation of higher order modes is shown. All simulations are based on a ridge width of $w_\mathrm{r} = 2.2$ µm. The presented results focus on the self-transmission $T_\mathrm{j,j}$ of the first three waveguide modes and the cross-coupling $T_\mathrm{1,j}$ from the fundamental to higher order modes ($j = 1, 2, 3$). Because of the small index step of the design the reflectance is negligible for all investigated structures.

Fig. 6 (a) shows results of the mode-size converter. Here, T_{11} and T_{13} are plotted as functions of the taper length L_t for different values of the taper width. It can be seen that to achieve a high T_{11} the taper needs to become longer if w_t is increased. To achieve a $T_{11} > 95\ \%$ the full opening angle

$\Theta_\mathrm{t} = \tan^{-1}(\frac{w_\mathrm{t}-w_\mathrm{r}}{L_\mathrm{t}})$ (see Fig. 3) has to be smaller than $5°$ whereas to ensure that the cross-coupling T_{13} is lower than 2%, Θ_t has to be smaller than $4°$.

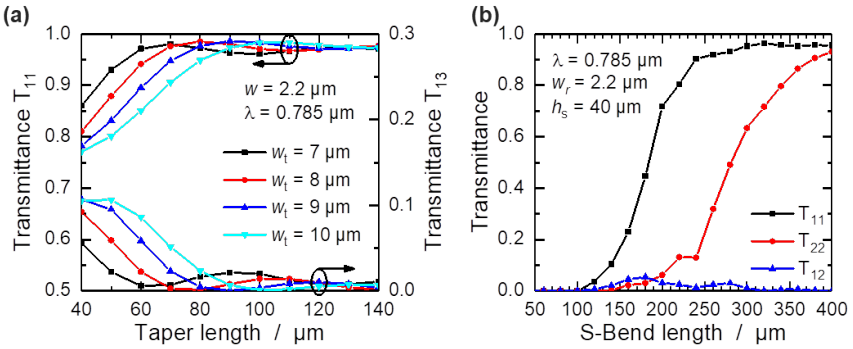

Figure 6: Transmittance of (a) the mode-size converter as function of the taper length for different taper widths and (b) the S-bend as function of the bend length.

The S-bend simulation results are shown in Fig. 6 (b). Here, the self-transmission of the first and second mode as well as their cross-coupling are plotted. T_{33} has been found to have high bend losses in the range of the investigated bend lengths and is thus omitted. It can be seen that the optimal bend length is a trade-off between having a high T_{11} and low cross-coupling T_{12} but still low second mode transmission T_{22}.

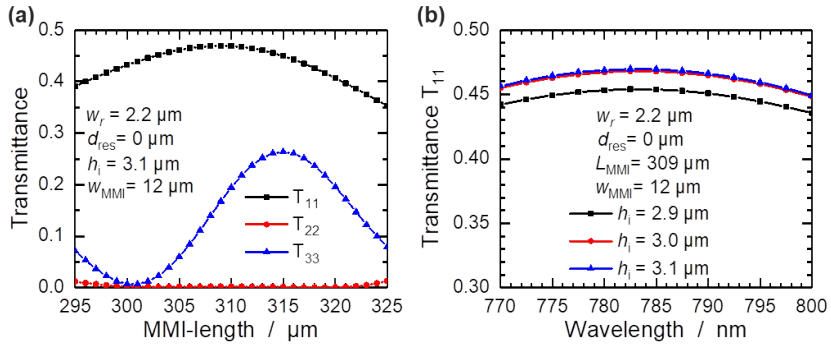

Figure 7: Transmittance of a 12 µm wide multi-mode interference (MMI) coupler (a) as function of its length and (b) as function of wavelength.

Fig. 7 shows the mode transmittance as function of the MMI length and the wavelength. Both plots show a maximal fundamental mode transmission of $T_{11} \approx 47\,\%$ at $L_\mathrm{MMI} = 309$ µm and $\lambda = 785$ nm if the device is used as depicted in Fig. 5. The left plot shows that the MMI efficiently acts as mode filter. At $L_\mathrm{MMI} = 309$ µm the transmission of the third mode is $\frac{T_{11}}{T_{33}} \approx 2.7$ times smaller than of the fundamental mode. The cross-coupling between modes was negligible small for all investigated values of L_MMI. Fig 7 (b) shows the low impact of wavelength on T_{11} for different values of the input waveguide offset h_i. Here, the maximal fundamental mode transmission T_{11} drop is only $4.5\,\%$.

5 Active device simulations

Based on the passive waveguide simulations presented in Section 4 the device geometry parameters were set to: $L_\mathrm{t} = 100$ µm, $w_\mathrm{t} = 8$ µm, $L_\mathrm{s} = 491$ µm, $h_\mathrm{s} = 40$ µm, $L_\mathrm{MMI} = 309$ µm and $w_\mathrm{MMI} = 12$ µm, leading to a CS length of 1000 µm. The MCS length was chosen to be $L_\mathrm{MCS} = 1750$ µm containing a DBR of 1000 µm length. Two FS lengths, 500 µm and 1000 µm, were investigated. The facet reflectivities were set to $0\,\%$ and $3\,\%$ at the rear and front facet, respectively.

In what follows we consider the case where only the upper of the two laser arms is electrically driven, applying voltages of 2.5 V, 1.7 V and 3.5 V to the gain sections of the MCS, CS and FS, respectively.

The corresponding areas are color-coded within Fig. 1. The CS voltage of 1.7 V was estimated to result in a carrier density slightly above transparency ($N_{\mathrm{tr}} = 1.4 \cdot 10^{24}$ m^{-3}). As mentioned in Section 3.2 the time averaged values were obtained between 2 ns and 3 ns after switching on all voltages.

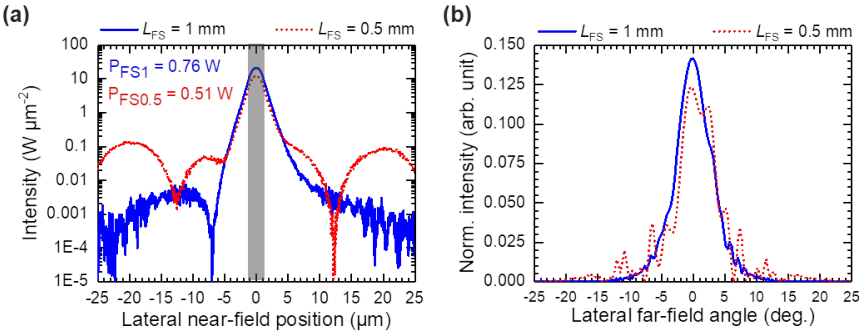

Figure 8: (a) Near- (logarithmic y-axis) and (b) far-field intensity profiles. Laser with long/short front section are shown as blue-solid/red-dotted lines.

Fig. 8 shows the near- and far-field intensity profiles obtained for devices having differently long FSs. Within and close to the waveguide (gray bar in panel (a)) both lengths of the FS lead to similar near-field profiles. Further away from the waveguide the laser with the shorter FS shows distinct side peaks. This, in turn, results in a modulated far-field profile.

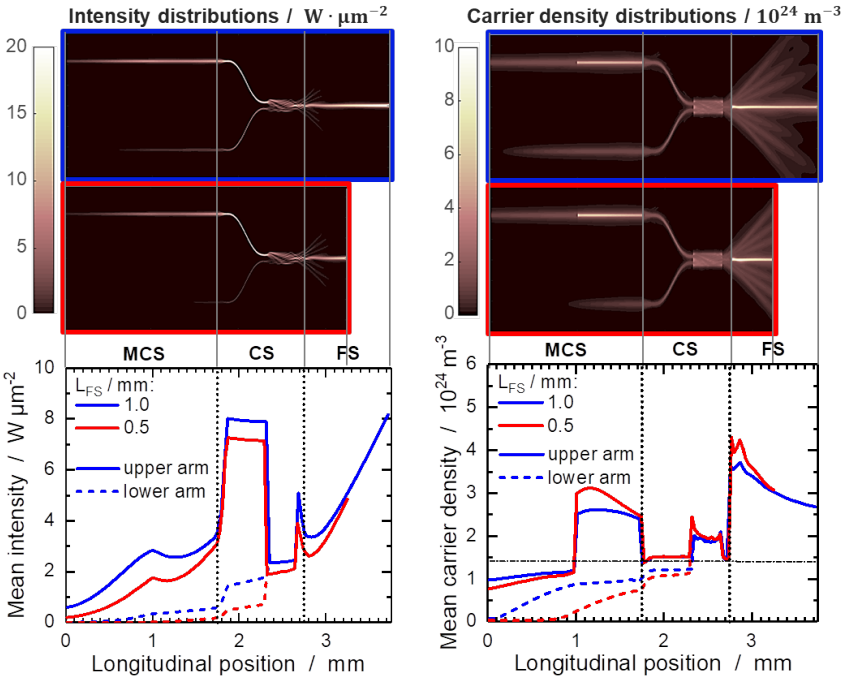

Figure 9: Top: Intensity (left) and carrier density (right) distributions. Bottom: Mean intensity (left) and carrier density (right) values within the upper (solid) and lower (dashed) laser arms.

The origin of this effect is visible from the distributions shown in the upper part of Fig. 9. A fraction of the guided light which propagates from the upper laser channel into the MMI is not coupled into the common output waveguide but radiated (cf. Fig. 5). This radiated light propagates further and eventually reaches the front facet leading to the modulated far field profile. Since the areas next to the waveguide are unbiased, the radiated light gets absorbed within the AR creating excess carriers until transparency is reached. This effect leads to a fan-like carrier density distribution within the FS, see upper right part of Fig. 9. In case of an FS length of 1000 µm most of the radiated light gets absorbed before reaching the front facet.

The bottom part of Fig. 9 shows the longitudinally resolved mean intensity and carrier density profiles within the upper (straight lines) and lower (dashed lines) laser arm. They were obtained by averaging the (z,x)-distributions over the width of the fundamental lateral guided mode w_0 at each longitudinal position. The width w_0 is defined as the distance between the two points of the mode profile that are equal to $1\ \%$ of its maximum intensity. Since both laser arms share a common front part of the resonator their mean values are identical within the MMI and FS. The mean intensity inside the biased upper arm increases within the MCS and FS indicating light amplification. The jump and subsequently drop of mean intensity within the CS is caused by the transition of low to high lateral confinement RWs and the change in waveguide width ($w_\mathrm{r} \Rightarrow w_\mathrm{MMI}$), respectively. Both mean distributions indicate that a part of the backward traveling light is coupled into the unbiased lower laser arm where it gets absorbed creating excess carriers. This happens within smaller distances for the laser with shorter FS. Nevertheless, both lasers provide negligible feedback from the lower unbiased laser arm back to the FS. As intended, the mean carrier density of the CS reaches values slightly higher than N_tr. Inside the MMI coupler, however, lateral spatial hole burning leads to an increased mean carrier density. Within the MCS and FS longitudinal spatial hole burning effects are visible which are more pronounced for the laser with short FS length.

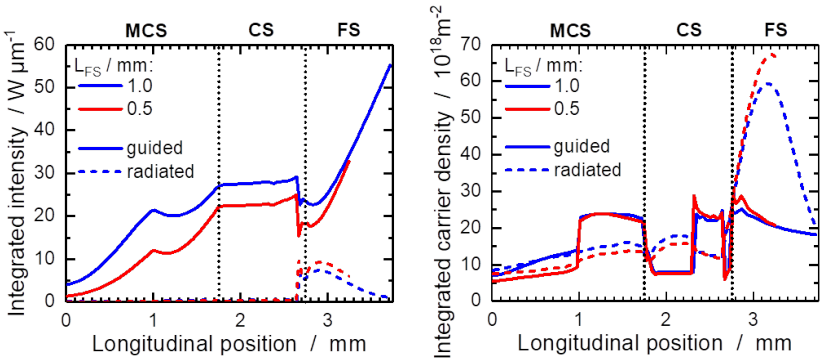

Figure 10: Integrated time averaged intensity (left) and carrier density (right) overlapping with guided (solid) and radiated (dashed) light at all longitudinal positions

Fig. 10 shows the integrated intensity and carrier density. The lateral integration limits were defined in the same way as before. It follows that the region between $-w_0/2$ and $w_0/2$ has a high spatial overlap with guided (straight lines) and the region outside this limits with radiated (dashed lines) light. In contrast to the bottom part of Fig. 9 where lateral *averages* of the corresponding (z,x)-distributions were shown, this representation shows lateral *integrals* of these distributions and does not resolve the individual laser arms. The integrated intensity inside the CS is nearly constant meaning that this section is optically transparent. However, behind the MMI a drop of the guided but a jump of the radiated integrated intensity can be seen. The latter gets absorbed during its propagation through the FS. Depending on the FS length, however, a higher fraction reaches the front facet. In the left part of Fig. 10 the effect of radiated light on the carrier density is visible. The number of carriers increases and reaches its maximum approximately 400 µm behind the CS. This results in a large number of carriers at the front facet in case of the short FS length. However, this is not the case for the long FS length. Here the integrated carrier density significantly drops after reaching its maximum.

6 Conclusion

The promising simulation results of our compact GaAs based tunable dual-wave-length laser system having two different etch depths, confirm our two stage design approach. Passive simulations were used to efficiently optimize integrated waveguide components, whereas active laser simulations have

proven to be vital to understand the internal light and carrier distributions within such devices. Compared to previous designs the coupler section length was reduced by one half to 1000 µm. Furthermore, we showed that a properly designed front section length can be used to avoid the appearance of far-field modulations by preventing that radiated light reaches the front facet. To keep the front section short, highly absorbing areas could be placed next to the front section waveguide to increase the absorption of radiated light.

Acknowledgements

The authors want to thank H.-J. Wünsche for the discussions contributing to this work.

References

[1] B. Sumpf, J. Kabitzke, J. Fricke, P. Ressel, A. Müller, M. Maiwald, G. Tränkle, “Dual-wavelength diode laser with electrically adjustable wavelength distance at 785 nm,” *Opt. Lett.* **41**, 3694-3697 (2016).

[2] T.N. Vu, A. Klehr, B. Sumpf, T. Hoffmann, A. Liero, G. Tränkle, “Pulsed hybrid dual wavelength Y-branch-DFB laser-tapered amplifier system suitable for water vapor detection at 965 nm with 16 W peak power,” in *Novel In-Plane Semiconductor Lasers XV*, p. 97670R. International Society for Optics and Photonics (2016)

[3] J.O. Gwaro, C. Brenner, B. Sumpf, A. Klehr, J. Fricke, M.R. Hofmann, “Terahertz frequency generation with monolithically integrated dual wavelength distributed Bragg reflector semiconductor laser diode,” *IET Optoelectronics* **11**, 49-52 (2017).

[4] R.K. Price, V.B. Verma, K.E. Tobin, V.C. Elarde, J.J. Coleman, “Y-branch surface-etched distributed Bragg reflector lasers at 850 nm for optical heterodyning,” *IEEE Photonics Technology Letters* **19**, 1610-1612 (2007).

[5] J. Fricke, A. Klehr, O. Brox, W. John, A. Ginolas, P. Ressel, L. Weixelbaum, G. Erbert, “Y-branch coupled DFB-lasers based on high-order Bragg gratings for wavelength stabilization,” *Semicond. Sci. Technol.* **28**, 035009 (2013).

[6] H. Wenzel, “Basic aspects of high-power semiconductor laser simulation,” *IEEE J. of Sel. Topics in Quantum Electronics* **19**, 1-13 (2013).

[7] A. Kumar, S. Aditya, “Performance of S-bends for integrated-optic waveguides,” *Microw. Opt. Technol. Lett.* **19**, 289-292 (1998).

[8] Photon Design®, “FIMMPROP - a powerful and versatile optical propagation tool” (2019). http://www.photond.com/products/fimmprop.htm. Accessed 15 August 2019

[9] D.F.G. Gallagher, T.P. Felici, “Eigenmode expansion methods for simulation of optical propagation in photonics: pros and cons,” in *Integrated Optics: Devices, Materials, and Technologies VII*, pp. 69-83. International Society for Optics and Photonics (2003)

[10] WIAS Berlin, “BALaser - a software tool for simulation of dynamics in broad area semiconductor lasers” (2019). http://www.wias-berlin.de/software/balaser/. Accessed 15 August 2019

[11] M. Radziunas, J. Fuhrmann, A. Zeghuzi, H.-J. Wünsche, T. Koprucki, C. Brée, H. Wenzel, U. Bandelow, "Efficient coupling of dynamic electro-optical and heat-transport models for high-power broad-area semiconductor lasers," *Opt. Quantum Electronics* **51**, 69 (2019).

[12] H.-J. Wünsche, M. Radziunas, S. Bauer, O. Brox, B. Sartorius, "Modeling of mode control and noise in self-pulsating PhaseCOMB lasers," *IEEE J. of Sel. Topics in Quantum Electronics* **9**, 857-864 (2003).

[13] C.Z. Ning, R.A. Indik, J.V. Moloney, "Effective Bloch equations for semiconductor lasers and amplifiers," *IEEE J. of Quantum Electronics* **33**, 1543-1550 (1997).

[14] A. Zeghuzi, M. Radziunas, H.-J. Wünsche, J. Koester, H. Wenzel, U. Bandelow, A. Knigge, "Traveling Wave Analysis of Non-Thermal Far-Field Blooming in High-Power Broad-Area Lasers," *IEEE J. of Quantum Electronics* **55**, 1-7 (2019).

[15] A. Zeghuzi, H.-J. Wünsche, H. Wenzel, M. Radziunas, J. Fuhrmann, A. Klehr, U. Bandelow, A. Knigge, "Time-dependent simulation of thermal lensing in high-power broad-area semiconductor lasers," *IEEE J. of Sel. Topics in Quantum Electronics* **25**, 1-10 (2019).